Acta Materialia 272 (2024) 119940

Contents lists available at ScienceDirect

Acta Materialia

journal homepage: www.elsevier.com/locate/actamat

Tensile creep behavior of the $Nb_{45}Ta_{25}Ti_{15}Hf_{15}$ refractory high entropy alloy

Gianmarco Sahragard-Monfared [a,1], Calvin H. Belcher [b,1], Sakshi Bajpai [b], Mark Wirth [c], Arun Devaraj [c], Diran Apelian [b], Enrique J. Lavernia [d], Robert O. Ritchie [e,f], Andrew M. Minor [e,f], Jeffery C. Gibeling [a], Cheng Zhang [b,2,*], Mingwei Zhang [a,e,f,*]

[a] Department of Materials Science and Engineering, University of California, One Shields Avenue, Davis, CA 95616, USA
[b] Department of Materials Science and Engineering, University of California, Irvine, California 92697, USA
[c] Pacific Northwest National Laboratory, 902 Battelle Blvd, Richland, Washington 99354, USA
[d] Department of Materials Science and Engineering, Department of Mechanical Engineering, Texas A&M University, College Station, TX 77840, USA
[e] Lawrence Berkeley National Laboratory, 1 Cyclotron Road, Berkeley, California 94720, USA
[f] Department of Materials Science and Engineering, University of California, 2607 Hearst Avenue, Berkeley, California 94720, USA

ARTICLE INFO

Keywords:
Creep
High-temperature deformation
Mechanism
Thermally activated processes
High-entropy alloys

ABSTRACT

The tensile creep behavior of a vacuum arc-melted $Nb_{45}Ta_{25}Ti_{15}Hf_{15}$ refractory high entropy alloy was investigated over a constant true stress range of 50–300 MPa at a temperature of 1173 K. Creep tests were carried out in both high vacuum (5×10^{-6} torr) and ultrahigh purity Ar gas to examine the environmental effect. The samples tested in vacuum exhibited power law behavior with a stress exponent of 4.1 and exceptional tensile creep ductility, whereas those tested in Ar suffered significant embrittlement due to HfO_2 formation at grain boundaries, which was exacerbated at low applied stresses where extended exposure to residual O_2 gas resulted in more extensive brittle intergranular fracture. Phase decomposition occurred after long-term thermal exposure, where a second Hf-rich body-centered cubic phase formed predominantly at grain boundaries but did not cause embrittlement. Compared to the equiatomic TaNbHfZrTi (Senkov alloy) and face-centered cubic multiple-principal element alloys, $Nb_{45}Ta_{25}Ti_{15}Hf_{15}$ has superior creep resistance, especially at high applied stresses, while maintaining excellent creep ductility. Transmission electron microscopy revealed that creep deformation in $Nb_{45}Ta_{25}Ti_{15}Hf_{15}$ at 1173 K is controlled by cross-kink collisions from screw dislocations that results in dipole drag at lower strain rates and jog drag at higher strain rates.

1. Introduction

Refractory high entropy alloys (RHEAs), also known as refractory multiple principal element alloys (RMPEAs), or refractory complex concentrated alloys (RCCAs), are a new class of alloys that consist of at least three principal elements (5–35 at.%) from Group IV-VI refractory metals (Ti, V, Cr, Zr, Nb, Mo, Hf, Ta, W) [1,2]. These alloys typically have body-centered cubic (BCC) crystal structures and are known for their high melting points above 2273 K and exceptional high temperature strength. For example, the CrMoNbV RHEA possesses a yield strength of 1.1 GPa at 1273 K [3] and the MoNbTaW and MoNbTaWV RHEAs can retain a yield strength of 500 MPa at 1873 K [4], which are unparalleled by any conventional alloy known to date. Therefore, the RHEAs have offered remarkable potential for developing new high temperature alloys that can surpass the operating temperatures of Ni-based superalloys for gas turbines with increased efficiency [5].

However, the widespread application of most RHEAs is significantly limited by their poor tensile ductility and fracture toughness, even above their ductile-to-brittle transition temperatures (DBTT) due to grain boundary embrittlement [4,6-8]. To date, the only known RHEA family that has extensive room temperature tensile ductility is the TaNbHfZrTi family (commonly referred to as the Senkov alloy) [9–11]. Notably, the

* Corresponding authors at: Department of Materials Science and Engineering, University of California, One Shields Avenue, Davis, CA 95616.
E-mail addresses: cheng_zhang@xjtu.edu.cn (C. Zhang), mwwzhang@ucdavis.edu (M. Zhang).
[1] G. Sahragard-Monfared and C.H. Belcher contributed equally to this paper.
[2] Current affiliation: Center for Alloy Innovation and Design, State Key Laboratory for Mechanical Behavior of Materials, Xi'an Jiaotong University, Xi'an 710049, China.

https://doi.org/10.1016/j.actamat.2024.119940
Received 18 January 2024; Received in revised form 22 March 2024; Accepted 16 April 2024
Available online 20 April 2024

high ductility of the Senkov alloy at cryogenic, room temperature, and high temperature while maintaining high strength in both tension and compression sets it apart from most other RHEAs and conventional BCC alloys. The mechanical properties of the Senkov alloy and several other BCC RHEAs have since been investigated with a focus on high-temperature properties for energy conversion systems and other applications in extreme environments [2,12]. However, the creep properties of RHEAs have only recently been reported in two studies by Liu et al. and Gadelmeier et al. [13,14]. These studies of RHEAs both investigated the Senkov alloy over different stress and temperature ranges and reported solute drag controlled dislocation creep at low stresses and dislocation climb controlled creep at high stresses through a phenomenological understanding of the stress exponents from power law creep [13,14]. The results are consistent with the creep behavior of other refractory alloys such as Ta - 2.5 wt.% W reported by Lin et al. [15]. As of yet, it is still unclear whether elevated-temperature creep deformation in the Senkov alloy family is controlled by motion of screw or edge dislocations, as recent research showed that edge dislocations can control the deformation in BCC RHEAs despite the well-known screw dislocation control in conventional BCC alloys [16–19]. In addition, the effect of interstitial constituents (especially O and N) on the creep behavior of RHEAs is still unknown. In a recent review paper, Belcher et al. [20] pointed out that the concentration of interstitial constituents and their potential segregation at grain boundaries have a critical impact on the mechanical properties of RHEAs. This becomes increasingly important for creep deformation, where the material is exposed at elevated temperatures for an extended amount of time and O can readily diffuse into the RHEAs from the surface since most of them do not form a dense layer of protective scale [21–25].

To broaden the understanding of creep in RHEAs through the first detailed mechanistic study of creep and environmental degradation, this investigation focuses on the tensile creep properties of a $Nb_{45}Ta_{25}Ti_{15}Hf_{15}$ RHEA. This composition is chosen based on published reports regarding the roles of various elements in refractory alloys [26] and is a modified version of an RHEA designed by Zhang et al. [27,28]. A high at. % of Nb was used because it has a low ductile to brittle transition temperature and a relatively low density. Ta and Ti were included to promote solid solution strengthening which is critically important for stable creep strength at high temperatures and Hf was utilized for grain boundary strengthening.

2. Experimental methods

The $Nb_{45}Ta_{25}Ti_{15}Hf_{15}$ RHEA was fabricated by arc-melting high-purity elemental refractory metals. The feedstock slugs and wires were all 99.95 % + purity by metals basis. Contamination during the arc-melting process was limited by pulling a vacuum of 1×10^{-5} torr on the chamber and then backfilling it with commercial purity Ar. Additionally, a Ti getter was melted in the chamber for 2 min before melting the $Nb_{45}Ta_{25}Ti_{15}Hf_{15}$ alloys to remove any residual O_2, N_2, and H_2O from the chamber and minimize interstitial impurities in the as-cast alloys. The arc-melted buttons were flipped and remelted five times without breaking the inert atmosphere to promote homogeneity. The material then underwent a 90 % thickness reduction via cold rolling to a final thickness of 0.6 mm and the rolled sheets were annealed at 1373 K for 1 hour, sealed in stainless steel bags to minimize the absorption of O and N during annealing. Dogbone-shaped tensile creep specimens with gauge section dimensions of 35.56 (L) x 2.54(W) x 0.6(T) mm^3 were then electrical discharge machined from the rolled sheets. All surfaces and edges of the gauge sections were polished using 600-grit SiC paper to minimize the possibility of surface defects influencing creep properties.

Constant stress tensile creep tests were performed at a temperature of 1173 K and stress range of 50–300 MPa with additional tests performed at temperatures of 1123 K and 1223 K and stresses of 100 MPa and 250 MPa to determine activation energies. To reduce oxidation during testing and compare the difference between different protective environments, creep tests were conducted in high vacuum as well as ultrahigh purity (UHP) Ar. The high vacuum environment and a corresponding closed system in principle provides better oxidation protection than Ar due to residual O_2 gas presence in UHP Ar backfilled systems. Additionally, the specimens were surrounded by Ti foil to getter any residual O_2 gas. For the creep experiments in UHP Ar, a vacuum of 3×10^{-5} torr was first pulled on the furnace chamber which was subsequently backfilled with a constant flow of Ar maintaining a slightly positive pressure above atmospheric to prevent O_2 gas from entering the chamber. The vacuum level for creep experiments in high vacuum was below 5×10^{-6} torr. All tests were conducted until fracture to clearly identify the steady-state creep rate except for one sample deformed in high vacuum with the lowest stress of 50 MPa, which was interrupted at 2×10^6 s during the steady-state creep regime. The determination of steady-state deformation is shown in **Supplementary Fig. 1,** where the creep rate has shown to stabilize at a constant, minimal value for more than 50 h. Before applying tensile stress, the furnace was stabilized at target temperatures for 3 h. The testing procedures described for this study are a modified version of those described in previous studies of face-centered cubic (FCC) materials which are less prone to oxidation [29–31].

Inert gas fusion was used to determine the composition of interstitial impurities O and N in the annealed, as-stabilized, and some selected post creep RHEA samples. Inert gas fusion was performed using an Eltra Elementrac ONH-p 2 analyzer with a maximum operating power of 6000 W. The samples were polished with 600 grit SiC paper and then sectioned into ~0.1000 g pieces for analysis using shears. From each RHEA sample, 3 pieces were analyzed to account for any statistical variation. For O and N analysis of the RHEAs, UHP He was used as the carrier gas and high purity Ni baskets with nibbled Ni pieces were used as the flux to fully remove and detect the N in the samples according to ASTM Standard E3346–22 [32].

Initial phase composition analysis was conducted using a Rigaku Ultima III X-ray Diffractometer (XRD) equipped with a Cu K_α (λ = 0.1542 nm) radiation source. The XRD was operated from 2θ angle of 20° - 100° at a voltage of 40 kV and current of 30 mA, a step size of 0.01° and speed of 2 steps per second. Before XRD analysis, the samples were mechanically polished up to 1200 grit SiC paper. XRD was used for initial phase composition analysis of the as-stabilized RHEA and some selected post-creep deformed RHEA samples. Scanning electron microscopy (SEM) was performed on a Thermo Fisher Quattro Environmental Scanning Electron Microscope (ESEM), an FEI Scios Dual Beam focus ion beam FIB/SEM equipped with an energy dispersive x-ray spectroscopy (EDS) detector as well as an FEI Quanta 3D FEG Dual Beam SEM/FIB equipped with an Everhardt-Thornley secondary electron detector, an Oxford Instruments EDS detector, and a pole piece mounted back scattered electron (BSE) detector. Electron backscatter diffraction (EBSD) analysis was performed using a Tescan GAIA 3 SEM-FIB. The cross sections of the RHEA samples were hot mounted in a conductive polymer and ground and polished to 0.05 μm colloidal silica. The cross sectioned samples were mounted such that electron micrographs could be captured normal to the rolling direction of the RHEAs. A Quattro ESEM was used in the backscatter electron mode to characterize the fracture surfaces of the specimens. The FEI Quanta 3D SEM was used to characterize atomic composition of metal constituent elements via EDS at an operating voltage of 20 kV. The grain orientations and boundary misorientations were analyzed via EBSD using the Tescan SEM at an operating voltage of 15 kV and step size of 0.3 μm. Grain size was determined from the EBSD grain boundary maps using the MTEX 5.10.2 grain diameter analysis in Matlab after removing unreasonably small grains and filled-in unindexed pixels based on neighboring pixel orientations.

Transmission electron microscopy (TEM) was conducted on a FEI ThemIS 60–300 S/TEM at an operating voltage of 300 kV and a JEOL 2100F S/TEM at an operating voltage of 200 kV using the diffraction contrast imaging-scanning transmission electron microscopy (DCI-

STEM) technique. $Nb_{45}Ta_{25}Ti_{15}Hf_{15}$ samples deformed at 50, 100, and 250 MPa under high vacuum were chosen for TEM, where the creep deformation was interrupted at the steady-state regime and the sample was furnace cooled under load to preserve the deformation microstructure. Samples for TEM analysis were cut from the gauge section of the creep specimens and ground to ~100 μm in thickness with a 1200-grit surface finish before 3 mm discs were punched out and twin-jet electropolished in a 10 vol% H_2SO_4 and 90 vol% methanol solution under −35 °C. The specimens were tilted to two-beam conditions near [111] zone axis for DCI-STEM imaging under low-angle annular dark field (LAADF). Additional TEM samples for grain boundary secondary phase examination were prepared by a standard FIB lift-out technique at 30 kV followed by 5 kV and 2 kV polishing to mitigate Ga-ion damage.

Site-specific needle samples from grain boundaries for atom probe tomography (APT) analysis was prepared by FIB lift-out and annular milling using a Thermo Fisher Scientific Helios Nanolab 600 FIB. The APT analysis was performed on a CAMECA LEAP 5000 XR APT system using laser assisted mode with 80 pJ laser pulse energy, 125 KHz pulse frequency, while sample temperature was maintained at 40 Kelvin and evaporation rate was maintained at 0.005 atoms/pulse. The APT data was reconstructed and analyzed using AP Suit software from CAMECA instruments.

3. Results and discussion

3.1. Characterization of initial microstructure

Many RHEAs have been observed to form a single BCC phase, yet some compositions result in two-phase BCC structures or dual-phase alloys consisting of BCC regions and intermetallic regions such as Laves, $L1_2$, B2, and sigma phases [2]. However, previous studies by Zhang et al. of alloys such as $Nb_{55}Ta_{25}Ti_{15}Hf_5$ [27] and $Nb_{40}Ta_{25}Ti_{15}Hf_{15}Zr_5$ [28] that are similar to the materials examined in this work have used X-ray diffraction to determine the presence of a single-phase BCC structure in arc melted, cold rolled, then recrystallized alloys. It is known that as-cast RHEAs are susceptible to elemental segregation formed during the solidification processes [1,33]. However, multiple studies, including those by Zhang et al., have determined that relatively low annealing temperatures and times can be used to homogenize RHEAs that have had significant thickness reductions (e.g., by cold rolling) after casting [27,28,33]. Conversely, as-cast RHEA specimens without further processing require relatively high annealing temperatures and times for elemental homogenization due to extremely low diffusion rates of the refractory constituents [27,28,33]. Therefore, several techniques were used to characterize the initial microstructure of $Nb_{45}Ta_{25}Ti_{15}Hf_{15}$ before creep testing as illustrated in Fig. 1. The tensile creep specimen has equiaxed grains with an average grain size of 30.4 μm and standard deviation of 32.3 μm across 1096 grains, and minimal texture in the gauge section, as illustrated by the EBSD inverse pole figure (IPF) color map (Fig. 1**b**). A single BCC phase was confirmed by both the EBSD data and XRD shown in Fig. 1**c**. Fig. 1**d, e** give the SEM secondary electron (SE) micrograph of the alloy as well as the corresponding EDS map, where no significant segregation and phase separation were discovered. However, significant segregation of oxygen at the grain boundaries (GBs) was detected by APT (region I in Fig. 1**f, g**), which is accompanied by the local depletion of Nb and Ti and local surge of Ta immediately near the GB (region II, 0–10 nm away from GB) and increasing/decreasing gradients of Ta/(Nb,Ti) further away from the GB (region III, 10–40 nm away from GB). It has recently been reported [34] that O can drive the formation of ordered O complexes (OOCs) and spinodal decomposition of the main BCC phase in some RHEAs due to the difference of O affinity and solubility for different refractory elements. Lei et al. [34] found a 48 % increase in ultimate tensile strength and 95 % increase in ductility after doping 2 at.% of O in an equiatomic

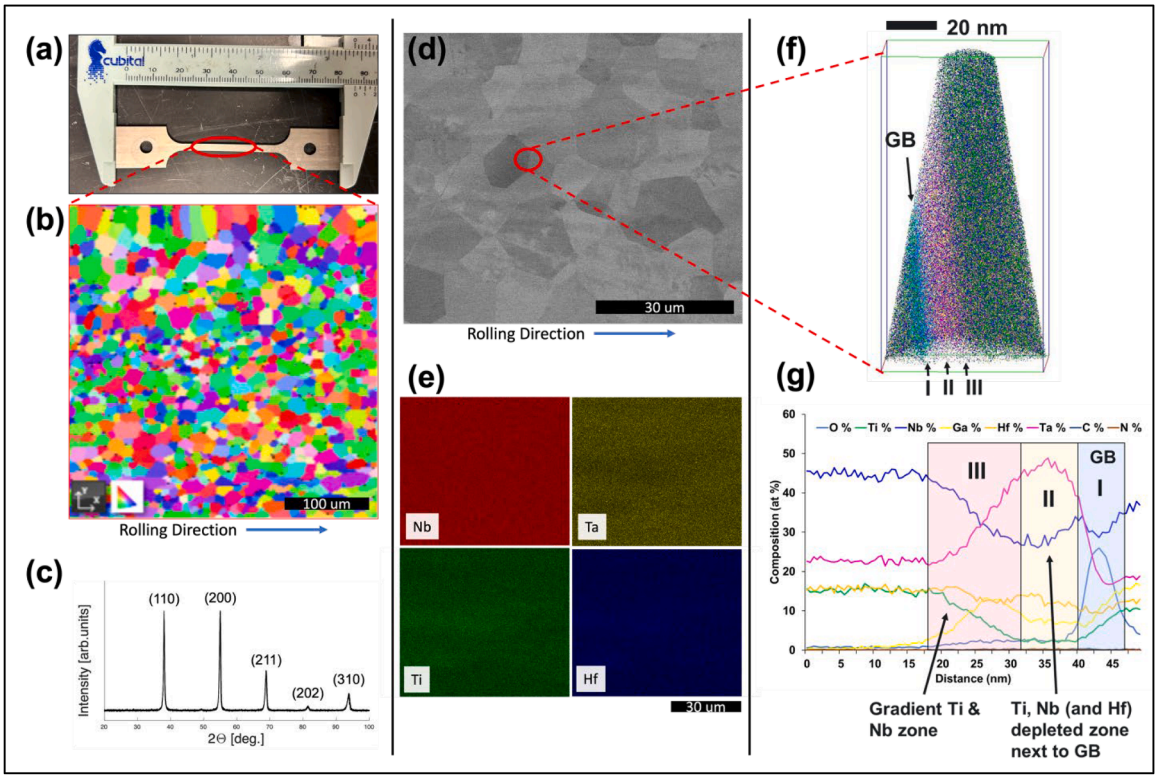

Fig. 1. Characterization of initial microstructure of $Nb_{45}Ta_{25}Ti_{15}Hf_{15}$ before creep testing. (a) shows the dogbone tensile creep specimen with a gauge length of 35.56 mm and a total length of ~80 mm. EBSD inverse pole figure (IPF) color map in (b) gives the grain structure in the cross-section of the material. XRD data in (c) shows a single BCC phase. SEM secondary electron (SE) image in (d) and corresponding EDS in (e) reveal a uniform distribution of the main constituents in the recrystallized alloy, whereas APT data in (f, g) show segregation of the main constituents and oxygen near a grain boundary.

TiZrHfNb RHEA. Such considerable enhancement of the mechanical properties was attributed to the formation of (O, Zr, Ti)-rich OOCs that are promoted by chemical short-range ordering of the main constituent elements. In a separate study, Cui et al. [35] discovered O-assisted spinodal decomposition of the matrix BCC phase of $Ti_{41}V_{27}Hf_{15}Nb_{15}O_2$ caused by the spinodal gap of (Ti, Hf) against Nb further extended by O doping. However, both phenomena were reported in bulk samples where 2 at.% O atoms were intentionally doped, which is a much higher concentration compared to our samples (349 ppm from the as-processed material or processing without intentional O doping, as shown in inert gas fusion data given later in *Section 3.3*). In our $Nb_{45}Ta_{25}Ti_{15}Hf_{15}$ RHEA, neither OOCs nor spinodal decomposition were detected after recrystallization, and the O and refractory elemental segregations were considered to be driven by GBs. Furthermore, the segregated O shown in APT was determined to be in the disordered form instead of forming oxides according to SEM and STEM nanodiffraction GB analysis that showed the absence of GB oxides.

3.2. Creep results and comparison of HEA creep behavior

Creep deformation of metals and alloys is typically distinguished by the primary, secondary, and tertiary regions. Primary creep corresponds to the buildup of dislocation density, secondary creep is interpreted as steady-state deformation; creep rate in this region remains constant, and tertiary creep is characterized by increasing creep rates due to the formation and coalescence of microcracks and voids [36]. The secondary creep is commonly described by the power law equation, where the relationship between the steady-state creep rate (or secondary creep rate), $\dot{\varepsilon}_{SS}$ and applied stress, σ, is given in Eq. (1). A is a material constant that includes the dislocation structure and elastic properties, Q_C represents the creep activation energy, R is the gas constant, and T is temperature [37]:

$$\dot{\varepsilon}_{SS} = A\sigma^n exp\left(-\frac{Q_C}{RT}\right). \quad (1)$$

A double logarithmic plot of the relationship between steady-state creep rates at 1173 K, which were calculated from the slopes of the secondary region of the creep curves, and applied stresses is illustrated in Fig. 2**a** to determine the stress exponent of this material in the tested stress range. Interestingly, the samples crept in high vacuum and Ar showed different power law behavior. A constant stress exponent of 4.1 was obtained for vacuum samples, whereas two stress exponents were observed for Ar samples, suggesting different creep deformation mechanisms at low and high applied stresses. Specifically, a stress exponent of 1.2 was found for the low applied stress region of 50–150 MPa while a stress exponent of 5.7 was observed for the high applied stress region of 200–300 MPa. In the framework of the power law creep model, the stress exponent of 1.2 is typically associated with creep deformation controlled by diffusion ($n = 1$ for lattice diffusion and $n = 2$ for grain boundary diffusion or sliding) and the stress exponent of 5.7 is in the range commonly associated with the dislocation climb mechanism of creep deformation ($n = 4$–6) [38]. Two stress exponents were also observed by Gadelmeier et al. [14] in a constant tensile load creep study of the Senkov alloy, with an exponent n ~ 2 at low applied stresses and an exponent in the range associated with dislocation climb controlled creep at high applied stresses. Liu et al. [13] also conducted a constant tensile load creep study of the Senkov alloy for small applied stresses and found an average stress exponent of $n = 2.6 \pm 0.1$, which is between the common ranges for grain boundary sliding and solute drag controlled creep ($n = 3$) according to the power law creep model. It is important to note that the grain size in the work of Liu et al. is much larger than that in the study by Gadelmeier et al. However, with a stress exponent between the typical values for grain boundary sliding and solute drag controlled creep, it is difficult to determine if the larger grain size caused this difference from the grain boundary sliding reported by Gadelmeier et al. [13,14].

The interpretation of the results for Ar samples through phenomenological understanding of creep data in conventional alloys is further obfuscated by the fact that diffusional creep, either through the lattice (typically occurs above 0.8 T_m) or through grain boundaries (typically occurs above 0.6 T_m and with fine grain sizes) [38], is unlikely to be observed in coarse grained $Nb_{45}Ta_{25}Ti_{15}Hf_{15}$ at the testing temperatures in this study (below 0.5T_m). Information in **Supplementary Fig. 2** further excludes the possible formation of small grains by dynamic recrystallization or twins and kink bands that were reported to form at lower temperatures and higher strain rates [10,11]. Fig. 2**b** shows Arrhenius plot that extracts the activation energy of creep for samples tested in vacuum, where a value of 253 kJ/mol was obtained. Although the activation energy for vacancy diffusion in $Nb_{45}Ta_{25}Ti_{15}Hf_{15}$ is still unknown, that for similar Senkov alloys was shown to be 238 kJ/mol via grain growth data [39]. Therefore, creep in $Nb_{45}Ta_{25}Ti_{15}Hf_{15}$ is likely to be controlled by dislocation mechanisms associated with vacancy diffusion, which is elaborated in *Section 3.4* with TEM results.

Fig. 3 shows a comparison of the steady-state creep rates (or minimum creep rates) of a variety of HEAs and a Ni-based superalloy. It is noted that the creep resistance of $Nb_{45}Ta_{25}Ti_{15}Hf_{15}$ is superior to that of the Senkov alloy [13,14] and a widely studied FCC HEA, CrCoNi, in both

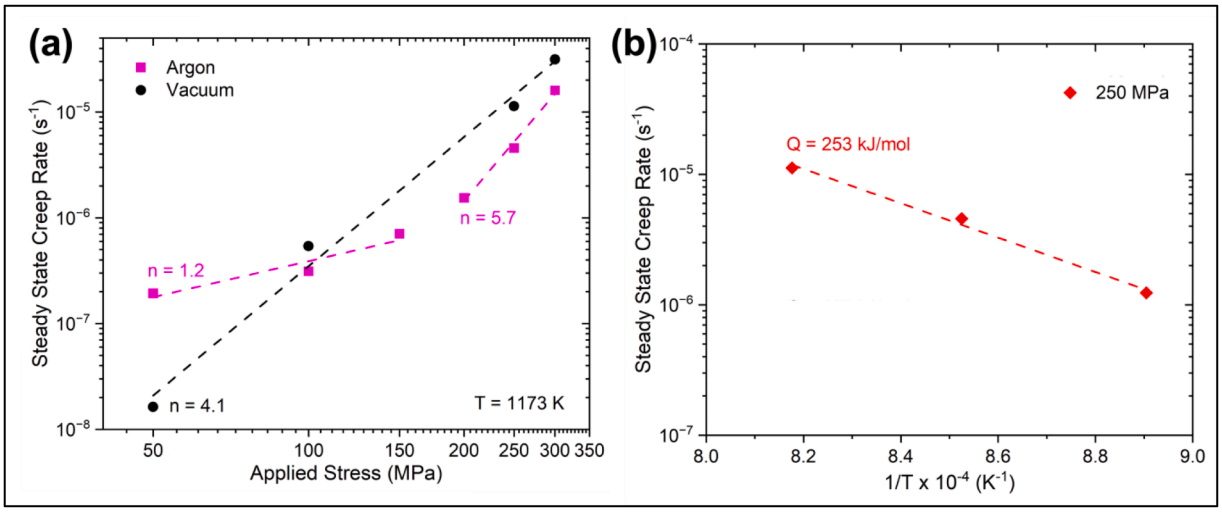

Fig. 2. (a) Steady-state creep rates of $Nb_{45}Ta_{25}Ti_{15}Hf_{15}$ as a function of stress for specimens crept at 1173 K in vacuum (circle) and in argon (square); (b) Arrhenius plot of logarithmic creep rate as a function of inverse temperature that gives an activation energy of 253 kJ/mol for the samples tested in vacuum.

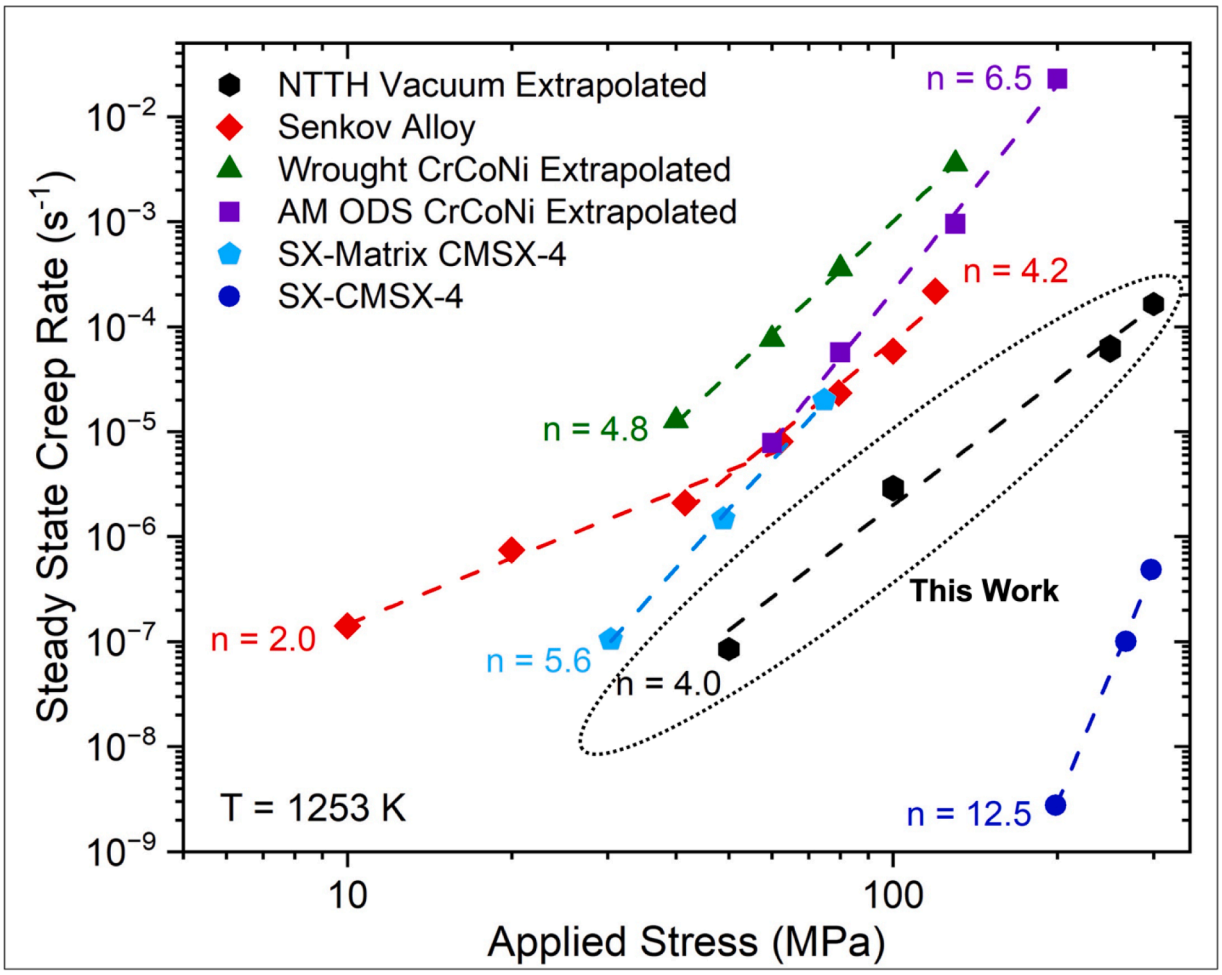

Fig. 3. Comparison of steady-state creep rates among several different types of HEAs: BCC $Nb_{45}Ta_{25}Ti_{15}Hf_{15}$ (or NTTH investigated in this study), TaNbHfZrTi (or the Senkov alloy [13,14]), wrought FCC CrCoNi [30], additively manufactured (AM) oxide dispersion strengthened (ODS) CrCoNi [31], a commercial single crystal FCC/$L1_2$ two-phase Ni-based superalloy CMSX-4, as well as the FCC matrix of CMSX-4 (also a concentrated solid solution) [40]. The creep data were either reported at 1253 K or extrapolated to 1253 K using known activation energies for creep.

wrought form [30] and even an additively manufactured oxide dispersion strengthened (ODS) form with yttria addition [31]. Nonetheless, the single-phase BCC $Nb_{45}Ta_{25}Ti_{15}Hf_{15}$ is still less creep resistant than CMSX-4, a high-performance single crystal Ni-based superalloy, although the BCC $Nb_{45}Ta_{25}Ti_{15}Hf_{15}$ is more creep resistant than the FCC matrix of CMSX-4 without $L1_2$ γ' intermetallics [40]. Therefore, second phase strengthening is desired to further strengthen the ductile BCC RHEA matrix to improve the creep properties to compete with Ni-based superalloys and is referred to future work.

3.3. *Environmental effects on creep deformation and fracture*

It is known that UHP Ar testing systems (an open system) suffer from an O ingress [41] and will have a higher O_2 residual gas partial pressure in the chamber than vacuum furnaces (a closed system). The discrepancy in the stress exponents for samples deformed in vacuum and in Ar is likely due to an environmental effect, where excessive oxidation can cause cracking that elevates the creep rate [42]. This will lead to an overestimation of the "steady-state creep rate" because the minimum creep rate was actually collected in the tertiary region, which is more problematic for low applied stresses because of the longer exposure time to the environment. This effect is clearly illustrated in Fig. 4**a, b**, where a drastic difference is shown between the samples deformed in Ar and in vacuum under 50 and 100 MPa, the two lowest stresses applied to the samples in this study. First, a large decrease in creep ductility and time to fracture is observed for samples tested in Ar under both stresses. Second, the insets show that tertiary creep occurs prematurely for Ar samples, where a steady-state creep region between primary creep and tertiary creep cannot be clearly identified. Third, a much smaller primary creep strain is observed for Ar samples, especially under 50 MPa, which is likely due to strengthening by the oxides formed during the three-hour equilibration of the furnace at 1173 K before loading. In addition, it can be seen from Fig. 4**a, b** that true steady-state creep for samples in high vacuum was achieved at ~2×10^6 s (more than 3 weeks) for the 50 MPa sample and ~5×10^5 s (about 6 days) for the 100 MPa sample. Long testing times are necessary to properly extract steady-state creep data for this material. Fig. 4**c** gives the creep ductility at fracture for samples deformed in vacuum and in Ar, where exceptional creep ductility is shown for the vacuum samples (25 – 40 %) and significantly lower ductility is observed for the Ar samples (below 15 %).

Evidence of significant oxidation of the Ar samples and its implications on creep fracture of $Nb_{45}Ta_{25}Ti_{15}Hf_{15}$ is shown in Fig. 5. SEM-EDS on the side of the gauge section of a sample fractured under 50 MPa in Ar at 29 h in Fig. 5**a** shows enrichment of O at the edges of the crack which may have diffused through the sample along grain boundaries. Fig. 5**b, c** illustrates the fracture surface of samples crept in Ar under 100 MPa and 250 MPa, respectively. The sample deformed under 100 MPa also had a time to fracture of ~29 h (similar to the 50 MPa sample although the stress is twice as large), highlighting the dominance of brittle intergranular fracture caused by oxidation throughout the entire fracture

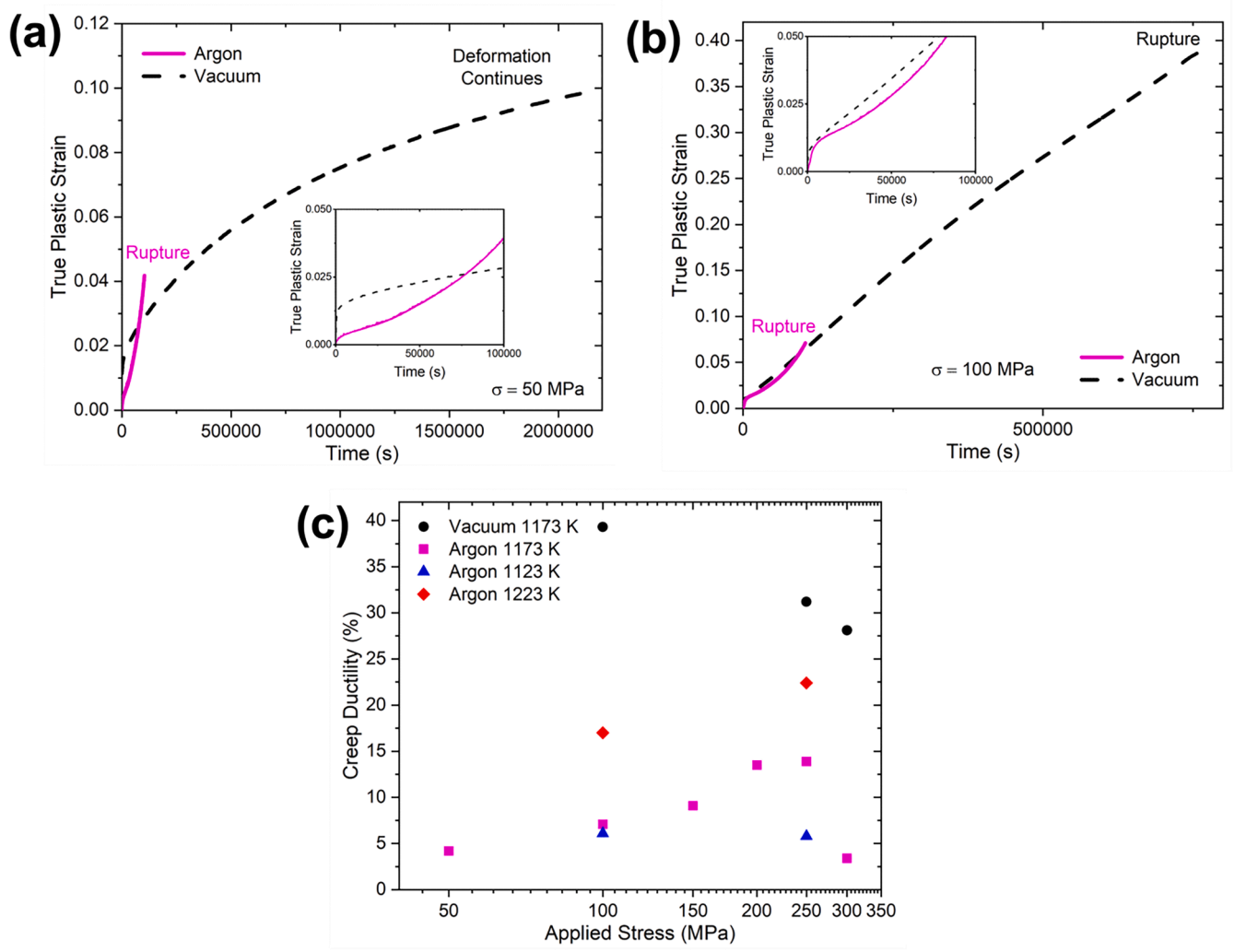

Fig. 4. Creep curves (true plastic strain as a function of time) for $Nb_{45}Ta_{25}Ti_{15}Hf_{15}$ under (a) 50 MPa and (b) 100 MPa for specimens crept at 1173 K in vacuum (dashed line) and in Ar (solid line). The insets show the first 100,000 s of creep deformation. (c) Creep ductility at fracture for samples deformed in vacuum or in Ar.

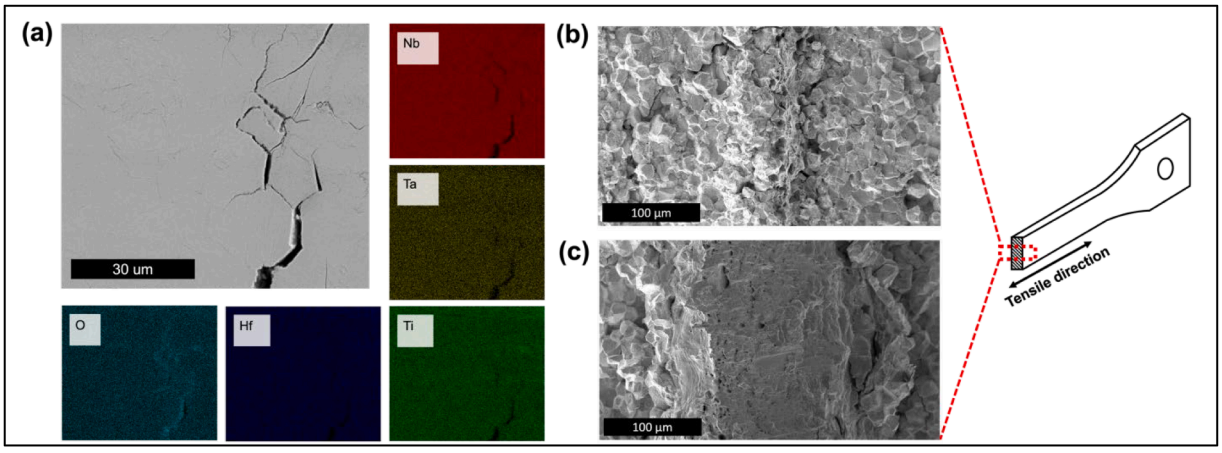

Fig. 5. (a) Side view of the sample gauge section that shows the crack propagation in $Nb_{45}Ta_{25}Ti_{15}Hf_{15}$ ruptured under 1173 K and 50 MPa in Ar, which illustrates intergranular fracture. Corresponding EDS maps show oxygen segregation near the cracks. (b) 1173 K and 100 MPa showing predominantly intergranular fracture. (c) 1173 K and 250 MPa showing intergranular fracture near sample surface and ductile fracture in the interior of the sample.

surface. When a higher stress of 250 MPa was applied for a reduced time to fracture of 4.5 h, O did not have enough time to diffuse through the entire cross-section since the interior of the sample shows dimples and ductile fracture whereas brittle intergranular fracture only prevails near the surfaces of the sample.

Although creep data suggest that oxidation is much less severe in creep samples tested in vacuum, XRD data in **Supplementary Fig. 3** clearly indicates the formation of HfO_2 (peaks at 2θ angles of ~ 28° and 31°) [43] for the sample deformed under 100 MPa at 1173 K and fractured after a significantly longer time - 216 h (~7.5 times longer than the sample tested in Ar under the same stress and temperature). Fig. 6 shows the SEM image of the cross-section of the 100 MPa sample, where two distinct features can be observed; the grey SEM-BSE contrast at grain boundaries near the surface shows inward O diffusion which led to HfO_2 formation as indicated by the EDS maps in Fig. 6**b,** revealing O enrichment. On the other hand, the white contrast in the sample interior signifies the formation of a secondary BCC phase that is rich in Hf. **Supplementary Fig. 4** gives the TEM selected area diffraction data for a FIB lift-out sample that contains the secondary BCC phase at a grain boundary, which confirmed the BCC crystal structure with a similar lattice constant to the matrix. In addition, it is noteworthy that the formation of HfO_2 can also explain the difference in the creep behavior for samples deformed in vacuum and in Ar in the high stress regime. In Fig. 2, the creep data for samples in Ar under higher stresses exhibit a higher stress exponent and a lower creep rate compared to the samples in vacuum. Both phenomena resemble those for oxide dispersion strengthening, where an increase in stress exponents and a decrease in creep rates are often observed [44].

This phase separation is well known in the Senkov alloy system, where the incompatibility between BCC-forming elements (Nb, Ta) and HCP-forming elements (Hf, Zr) drives a miscibility gap at intermediate temperatures [11,45]. However, this grain boundary phase separation does not seem to cause severe embrittlement that compromises the creep ductility of the material examined in this study, as Fig. 4 shows that the ductility increases with decreasing applied stress and prolonged thermal exposure for vacuum samples, a trend contrary to the sample tested in Ar. Similar microstructure was observed for the 50 MPa test over a duration of 555 h. The microstructure of the sample deformed under 50 MPa is provided in **Supplementary Fig. 5.**

When the RHEA was subjected to 250 MPa in vacuum over a duration of 4 h, the SEM investigation shown by Fig. 7 illustrates little evidence that grain boundary phase separation occurred compared to the 50 MPa and 100 MPa tests. Similar conclusions can be drawn for the 300 MPa test over a duration of 1.4 h. The microstructure of the sample deformed under 300 MPa is given in **Supplementary Fig. 6**.

Therefore, it can be concluded that the environmental effect plays a critical role in the creep properties of the $Nb_{45}Ta_{25}Ti_{15}Hf_{15}$ RHEA. As shown in Table 1, additional inert gas fusion experiments further confirmed that the UHP Ar environment increased the O as well as the N content in samples at a much faster rate than vacuum, where oxygen reached ~4000 ppm in 29 h for Ar samples and 216 h for vacuum samples. The N content also drastically increased for the sample crept in UHP Ar, although the formation of nitrides was not observed in the electron microscopy investigations.

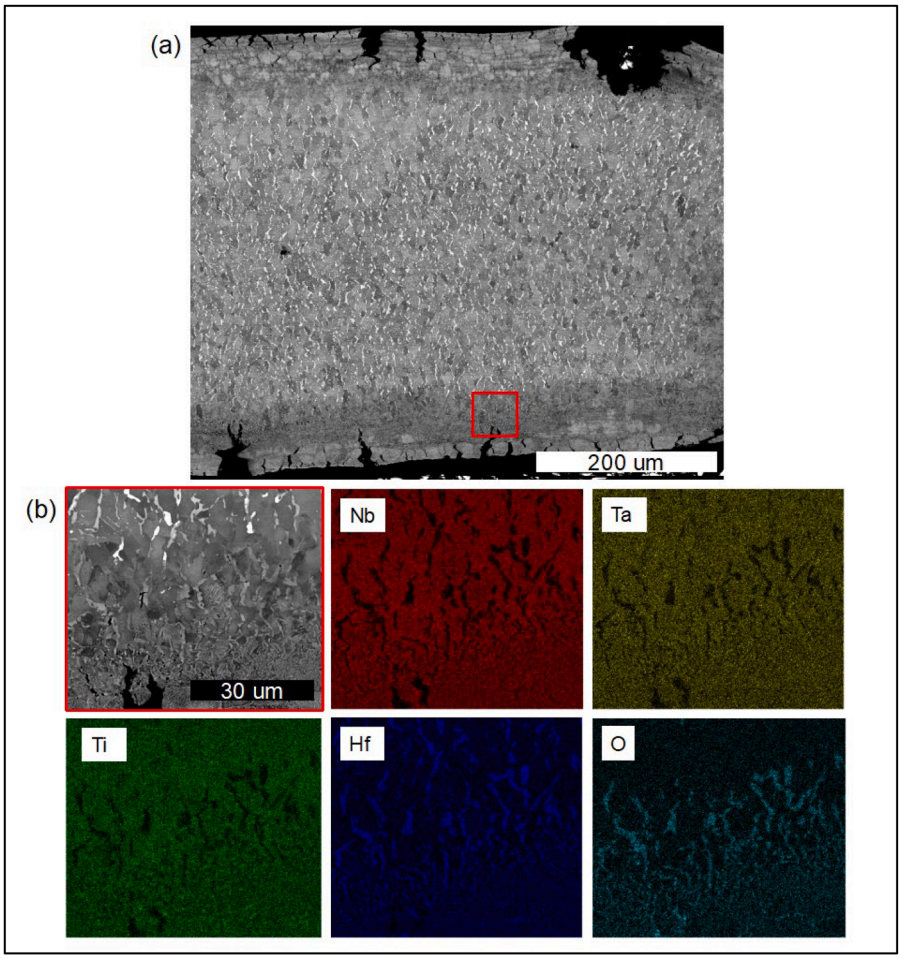

Fig. 6. (a) SEM-BSE image of the sample cross-section for $Nb_{45}Ta_{25}Ti_{15}Hf_{15}$ ruptured under 1173 K and 100 MPa in vacuum that reveals the formation of HfO_2 (grey contrast) near the surface and a second Hf-rich BCC phase at the sample interior. (b) Higher magnification BSE micrograph near the surface showing both the oxides and the secondary phase and corresponding EDS elemental maps for the BSE micrograph.

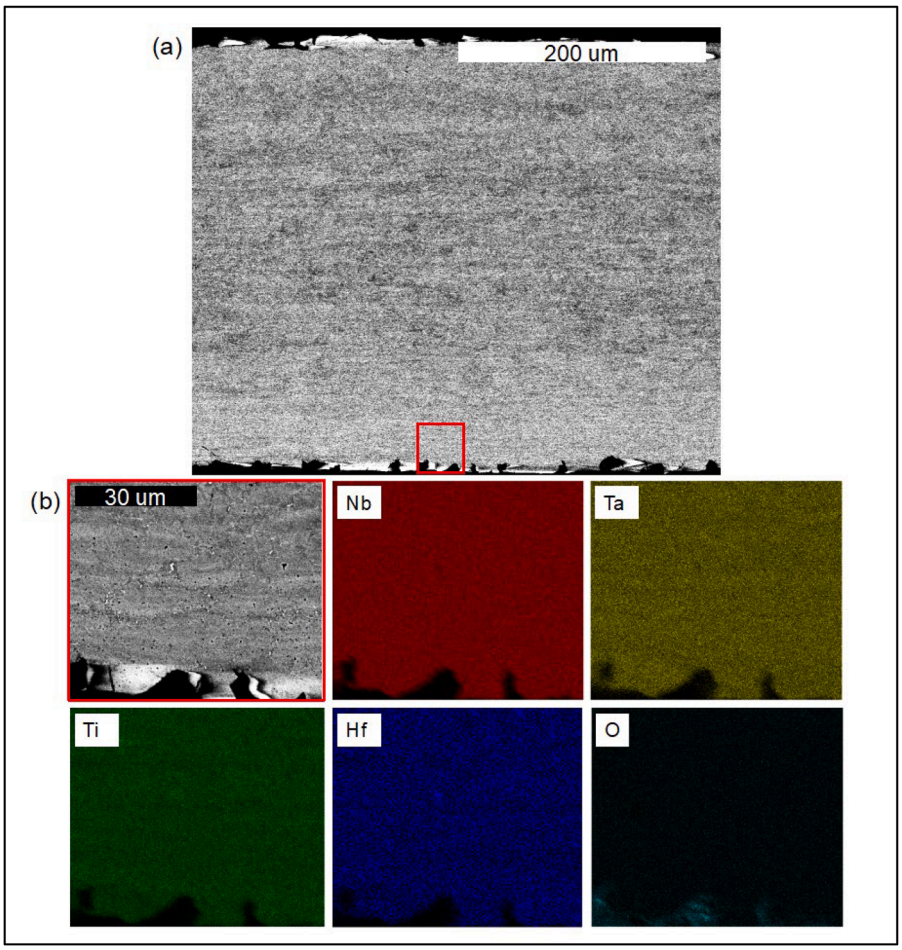

Fig. 7. (a) SEM-BSE image of the sample cross-section for $Nb_{45}Ta_{25}Ti_{15}Hf_{15}$ ruptured under 1173 K and 250 MPa in vacuum which reveals minimal oxidation near the surface (b) Higher magnification BSE micrograph near the surface showing little secondary Hf-rich BCC phase and corresponding EDS elemental maps for the BSE micrograph.

Table 1
Inert gas fusion data of oxygen and nitrogen in samples crept under a variety of conditions.

Condition	O [ppm]	N [ppm]
As-annealed 1373 K, 1 h	349 ± 53	171 ± 9
1173 K 3-hour stabilization before creep	404 ± 37	133 ± 4
100 MPa Creep, 1173 K in 10^{-6} torr, 216 h	4030 ± 169	150 ± 11
250 MPa Creep, 1173 K in 10^{-6} torr, 4 h	415	101
50 MPa Creep, 1173 K in Ar, 29 h	3826 ± 2342	1381 ± 235

3.4. Dislocation analysis and creep mechanisms

It is critical to understand the elevated temperature deformation mechanisms of $Nb_{45}Ta_{25}Ti_{15}Hf_{15}$ under creep strain rates lower than those used in tensile tests especially since the strain rate dependence of mechanical properties in BCC alloys is typically more important than that in their FCC counterparts [46]. It has been shown previously in this work that the activation energy of creep in $Nb_{45}Ta_{25}Ti_{15}Hf_{15}$ is consistent with that for vacancy diffusion. Combined with a stress exponent of 4, it is tempting to consider the classical edge dislocation climb-controlled creep to be the operating mechanism for this RHEA. However, multiple studies [47–50] have shown that plastic deformation in the Senkov alloy family is controlled by screw dislocations via cross-kink collisions, which contradicts climb of edge dislocations. Here, dedicated DCI-STEM was performed on samples crept under 50, 100, and 250 MPa in vacuum to elucidate the creep mechanisms of $Nb_{45}Ta_{25}Ti_{15}Hf_{15}$. Fig. 8**a** shows the steady-state creep microstructure of the 50 MPa sample, where long straight screw dislocations on (110) planes were observed. The slip planes of the dislocations can be determined by the g-vectors in the diffraction patterns, as the g-vectors in the reciprocal space is perpendicular to crystallographic planes in the real space. In Fig. 8**a**, although the sample was tilted to $g = [0\bar{1}1]$ two-beam condition, another two $\langle 110 \rangle$ diffraction peaks were still visible. The expanded view in Fig. 8**b** further reveals that the screw dislocations are accompanied by small "debris" (self-interstitial or self-vacancy loops), which is the signature feature of cross-kink collisions, where two kinks originated from the same screw dislocation migrate migrating on different {110} slip planes and collide with each other, forming a dislocation dipole. Further propagation of the dislocation relies on the diffusion of vacancies or interstitials to unlock the dipoles and thereby form vacancy or interstitial loops [51]. Therefore, dipole drag is the rate controlling step of deformation here, and the fact that the activation energy of creep obtained for $Nb_{45}Ta_{25}Ti_{15}Hf_{15}$ is equal to that for vacancy diffusion can be rationalized. In a recent molecular dynamics study [47], Zhou et al. showed that cross-kinks control screw dislocation motion in a NbTaV alloy from room to elevated temperatures, where the strength of the RHEA is characterized by screw dislocation self-pinning at low temperatures and cross-kink diffusion and annihilation at high temperatures. This is consistent with the deformation mechanism observed in our $Nb_{45}Ta_{25}Ti_{15}Hf_{15}$ RHEA at 1173 K. Although experimental and computational results have shown that deformation can be controlled by edge dislocations in a number of BCC RHEAs at elevated temperatures [17,52,53], including equiatomic MoNbTaW, CrMoNbW,

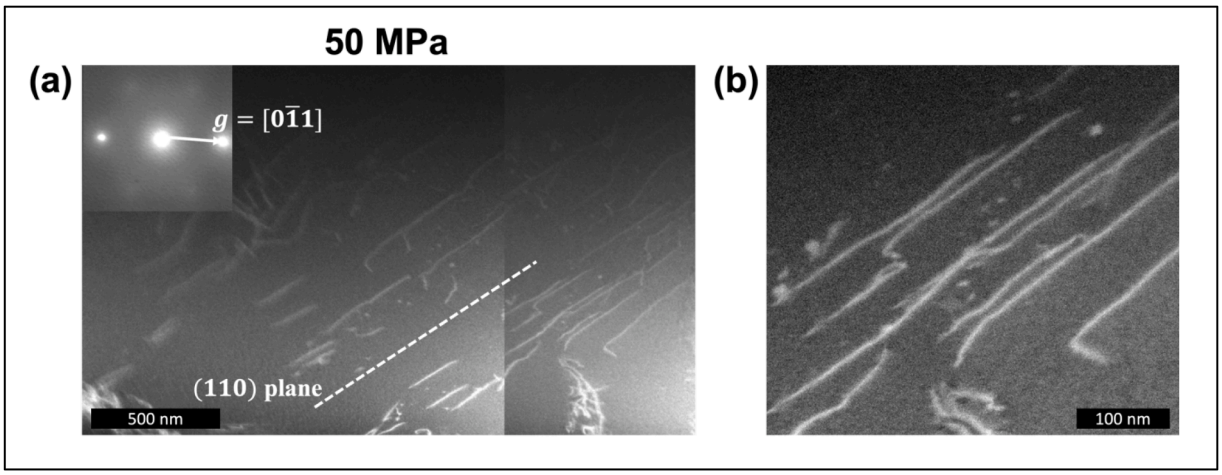

Fig. 8. (a) DCI-STEM image under a two-beam condition near [111] zone for the $Nb_{45}Ta_{25}Ti_{15}Hf_{15}$ sample crept under 1173 K and 50 MPa interrupted at steady-state deformation. The image was montaged for a larger field of view. (b) Expanded view of (a) showing the dislocation loops (debris) near screw dislocations.

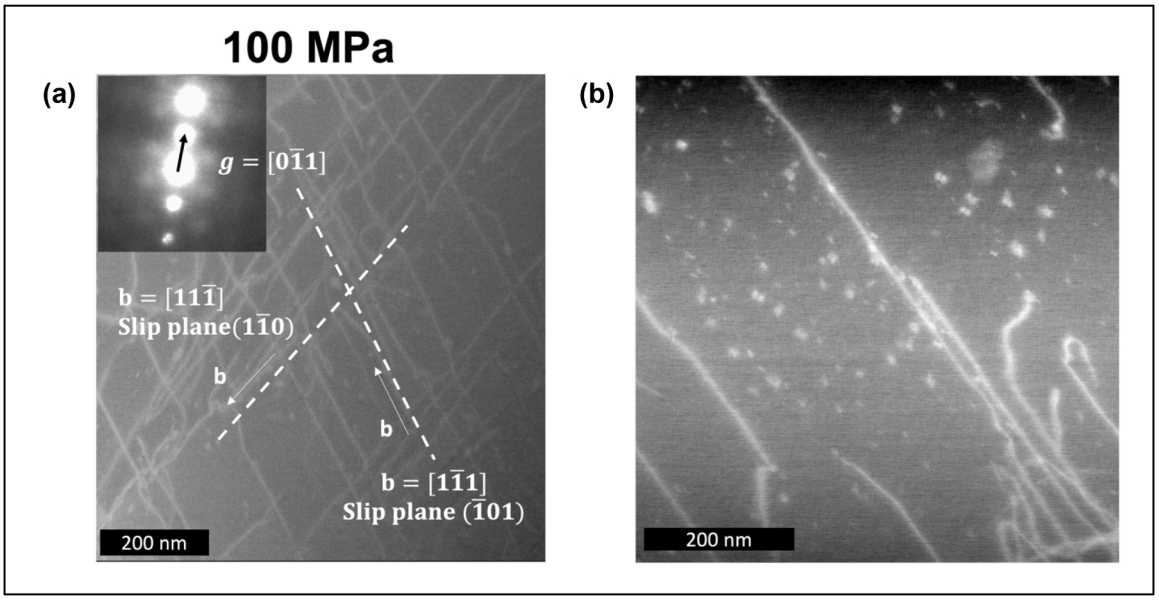

Fig. 9. (a) DCI-STEM image under a two-beam condition near [111] zone for the $Nb_{45}Ta_{25}Ti_{15}Hf_{15}$ sample crept under 1173 K and 100 MPa interrupted at steady-state deformation. A "**g** · **b**" analysis was performed for this condition (b) Expanded view of (a) showing the dislocation loops (debris) near screw dislocations.

and NbTaTiV, little evidence supports edge dislocation control in $Nb_{45}Ta_{25}Ti_{15}Hf_{15}$ under creep strain rates at 1173 K.

At the higher stress 100 MPa, a corresponding increase in dislocation density was observed as shown in Fig. 9**a**. Multiple slip systems were present for screw dislocations, where a "**g** · **b**" analysis was also performed to verify that the dislocations are indeed $(1\bar{1}0)[11\bar{1}]$ and $(\bar{1}01)[1\bar{1}1]$ screw dislocations. According to electron diffraction theory [54], the dislocation contrasts disappear when the g-vector corresponding to the specific two-beam condition is perpendicular to the Burgers vector (also known as "**g** · **b**" invisibility criterion). The STEM micrographs for the complete "**g** · **b**" analysis are given in the **Supplementary Fig. 7,** where the samples were tilted to six different two-beam conditions along two different zone axes to determine **b**. The higher magnification view in Fig. 9**b** again shows a large density of debris near the screw dislocations, where cross-kink collisions and dipole drag are again the rate-controlling deformation mechanisms.

It is interesting to note a change in the dislocation microstructure at the highest stress of 250 MPa in Fig. 10**a**, where debris was not observed. Instead, dislocations have a curvy and cusped morphology and appear to be pinned by objects that show black-white contrast in the STEM image. Creep in this regime is controlled by the motion of jogged screw dislocations, where the long screw segments are pinned by jogs with edge characters formed as a result of much more frequent cross-kink collision under a higher stress [50]. The black-white contrast shown at these pinning points is the indication of the tensile-compressive strain fields emanated from the cores of edge-on dislocations. The average spacing between the jogs was determined to be ~100 nm. When tilted to a different zone axis [100], Fig. 10**b** shows the jogged segments at the arrows, where the dislocations are pinned. Similar observations of jogged screw dislocations have been reported in other alloys, such as TiAl [55–57] and Zircaloy-4 [58] and modeled by Barrett et al. [59] and later modified by Viswanathan et al. [60], where a hyperbolic sine equation instead of the power law equation was used to model the relationship between the steady-state creep rate and the applied stress. Dedicated creep modeling is beyond the scope of the current paper because of the relatively few data points obtained from this study due to the difficulty of processing a large quantity of large creep samples.

It is important to compare the creep mechanisms of

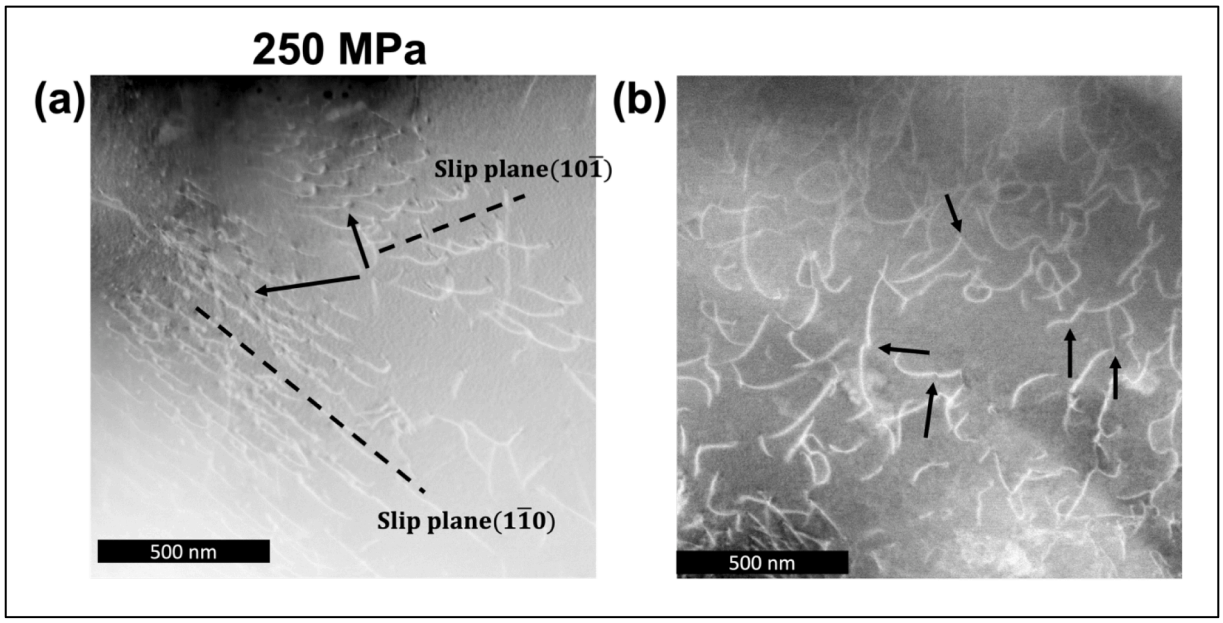

Fig. 10. (a) DCI-STEM image under a two-beam condition near [111] zone for the $Nb_{45}Ta_{25}Ti_{15}Hf_{15}$ sample crept under 1173 K and 250 MPa interrupted at steady-state deformation. (b) DCI-STEM image under a two-beam condition near [100] zone that shows the jogs as indicated by the arrows.

$Nb_{45}Ta_{25}Ti_{15}Hf_{15}$ with the recent plasticity theory of solid solution strengthening of BCC RHEAs developed by Rao et al. [50]. The theory states that the strength in some BCC RHEAs (mostly for the Senkov alloy family, including the alloy examined in this study for which deformation is based on a/2 <111> screw dislocation mobility) is controlled by dipole drag at low temperatures and jog drag at elevated temperatures. When the temperature is increased, enhanced bulk self-diffusion can collapse vacancy and interstitial dipoles, whereas jogs are still formed on the screw dislocation due to kink collisions with increased frequencies. It is shown in our study that the same mechanisms can be applied to creep as a function of strain rates at an intermediate temperature of 1173 K. At low strain rates below $10^{-6}\,s^{-1}$ (as a result of low applied stresses), the low kink collision rate and slow screw dislocation propagation will still result in dipole drag, when bulk diffusion in $Nb_{45}Ta_{25}Ti_{15}Hf_{15}$ at 1173 K is still not fast enough to annihilate the dipoles immediately. At higher strain rates $\sim 10^{-5}\,s^{-1}$, the increased kink collision rate and significant jog formation will take over, where jog drag becomes the dominant deformation mechanism. In a recent study, Cook et al. [61] revealed that at the tensile test strain rate of $10^{-3}\,s^{-1}$ up to 1473 K, the same $Nb_{45}Ta_{25}Ti_{15}Hf_{15}$ RHEA exhibits a drastic change in deformation mechanisms: deformation is controlled by the formation of edge dislocation-mediated kink bands (low angle boundaries) as well as the motion of dislocations of mixed characters, which induce significant tensile plasticity and give rise to massive fracture toughness. The results of this paper, combined with the study by Cook et al. [61], underscore the importance in the future investigation of the strain rate-dependent deformation behavior in NbTaTiHf-based RHEAs.

4. Conclusions

Constant stress creep tests at 1173 K in the stress range of 50–300 MPa were conducted on an arc melted, cold rolled, and annealed $Nb_{45}Ta_{25}Ti_{15}Hf_{15}$ RHEA to determine its creep behavior. The results for $Nb_{45}Ta_{25}Ti_{15}Hf_{15}$ were compared to the most creep resistant single-phase FCC MPEAs to date, CrCoNi, and the only other RHEA for which tensile creep data have been published, including the equiatomic TaNbHfZrTi (Senkov) alloy. The main findings of this study are summarized below:

1. Creep deformation in the $Nb_{45}Ta_{25}Ti_{15}Hf_{15}$ alloy at 1173 K was determined to be controlled by the motion of screw dislocations through cross-kink collision. At low strain rates (below 10^{-6} s^{-1}), creep is controlled by the dragging of vacancy/interstitial dipoles, where a large number of vacancy/self-interstitial dipoles were observed near the screw dislocations. At higher strain rates ($\sim 10^{-5}$ s^{-1}), creep is controlled by the dragging of jogs.
2. $Nb_{45}Ta_{25}Ti_{15}Hf_{15}$ has a superior creep resistance compared to the Senkov alloy and a representative FCC HEA, CrCoNi, even for its oxide dispersion strengthened form. However, the creep resistance of the RHEA is still inferior to that of CMSX-4, a high-performance commercial Ni-based superalloy. It is noted that the $Nb_{45}Ta_{25}Ti_{15}Hf_{15}$ is stronger than the FCC matrix of CMSX-4. Therefore, our results suggest the need for second-phase strengthening of the ductile BCC matrix, which can potentially result in RHEAs stronger than commercial Ni-based superalloys.
3. The creep properties of the $Nb_{45}Ta_{25}Ti_{15}Hf_{15}$ RHEA are extremely sensitive to the testing environments and the amount of oxygen present in the atmosphere. Creep samples tested in high vacuum exhibited excellent creep ductility, while the ductility drastically decreased when they were tested in ultrahigh purity Ar with O ingress. Oxidation occurred predominantly at grain boundaries that caused significant embrittlement through intergranular fracture. The formation of a second Hf-rich BCC phase at the grain boundaries after long term thermal exposure at 1173 K was also detected but determined not to be another cause of grain boundary embrittlement.

CRediT authorship contribution statement

Gianmarco Sahragard-Monfared: Data curation, Formal analysis, Investigation, Methodology, Software, Validation, Visualization, Writing – original draft, Writing – review & editing. **Calvin H. Belcher:** Data curation, Formal analysis, Investigation, Methodology, Resources, Visualization, Writing – review & editing. **Sakshi Bajpai:** Investigation, Validation, Visualization. **Mark Wirth:** Investigation, Validation, Visualization. **Arun Devaraj:** Funding acquisition, Supervision, Writing – review & editing. **Diran Apelian:** Conceptualization, Funding acquisition, Supervision, Writing – review & editing. **Enrique J. Lavernia:** Conceptualization, Funding acquisition, Supervision, Writing – review & editing. **Robert O. Ritchie:** Funding acquisition, Supervision, Writing

– review & editing. **Andrew M. Minor:** Funding acquisition, Supervision, Writing – review & editing. **Jeffery C. Gibeling:** Conceptualization, Funding acquisition, Supervision, Writing – review & editing. **Cheng Zhang:** Conceptualization, Resources, Writing – review & editing. **Mingwei Zhang:** Conceptualization, Data curation, Formal analysis, Investigation, Methodology, Project administration, Resources, Software, Supervision, Validation, Visualization, Writing – original draft, Writing – review & editing, Funding acquisition.

Declaration of competing interest

The authors declare that they have no known competing financial interests or personal relationships that could have appeared to influence the work reported in this paper.

Acknowledgements

Partial funding for this research was provided by the University of California, Davis and by donations to the Department of Materials Science and Engineering. A portion of this study was carried out at the UC Davis Center for Nano- and Micro-Manufacturing (CNM2) and the Advanced Material Characterization and Testing (AMCaT) Facility. Funding for the Thermo Fisher Quattro S was provided by NSF grant No. DMR-1725618.

Work at Lawrence Berkeley National Laboratory was funded by the U.S. Department of Energy, Office of Science, Basic Energy Sciences, Materials Sciences and Engineering Division, through the Damage-Tolerance in Structural Materials program (KC13) under contract no. DE-AC02-CH11231. Work at the Molecular Foundry was supported by the Office of Science, Office of Basic Energy Sciences, of the U.S. Department of Energy under Contract No. DE-AC02–05CH11231.

This research was partially supported by the National Science Foundation Materials Research Science and Engineering Center program through the UC Irvine Center for Complex Active Materials (DMR-2011967).

AD and MW would like to acknowledge the funding support for the APT sample preparation and APT analysis from U.S. Department of Energy, Office of Science, Basic Energy Sciences, Materials Sciences and Engineering Division as a part of the Early Career Research program (FWP # 76052). The FIB-based preparation of APT samples was conducted using facilities at Environmental Molecular Sciences Laboratory (EMSL), which is a DOE national user facility funded by Biological and Environmental Research Program located at Pacific Northwest National Laboratory.

Supplementary materials

Supplementary material associated with this article can be found, in the online version, at doi:10.1016/j.actamat.2024.119940.

References

[1] O.N. Senkov, G.B. Wilks, D.B. Miracle, C.P. Chuang, P.K. Liaw, Refractory high-entropy alloys, Intermetallics 18 (9) (2010) 1758–1765.
[2] O.N. Senkov, D.B. Miracle, K.J. Chaput, J. Couzinie, Development and exploration of refractory high entropy alloys—A review, J. Mater. Res. 33 (19) (2018) 3092–3128.
[3] R. Feng, B. Feng, M.C. Gao, C. Zhang, J.C. Neuefeind, J.D. Poplawsky, Y. Ren, K. An, M. Widom, P.K. Liaw, Superior High-Temperature Strength in a Supersaturated Refractory High-Entropy Alloy, Adv. Mater. 33 (48) (2021) 2102401.
[4] O.N. Senkov, G.B. Wilks, J.M. Scott, D.B. Miracle, Mechanical properties of Nb25Mo25Ta25W25 and V20Nb20Mo20Ta20W20 refractory high entropy alloys, Intermetallics 19 (5) (2011) 698–706.
[5] J.H. Perepezko, The Hotter the Engine, the Better, Science 326 (5956) (2009) 1068–1069.
[6] Z. Wang, H. Wu, Y. Wu, H. Huang, X. Zhu, Y. Zhang, H. Zhu, X. Yuan, Q. Chen, S. Wang, X. Liu, H. Wang, S. Jiang, M.J. Kim, Z. Lu, Solving oxygen embrittlement of refractory high-entropy alloy via grain boundary engineering, Mater. Today 54 (2022) 83–89.
[7] X. Li, W. Li, D.L. Irving, L.K. Varga, L. Vitos, S. Schönecker, Ductile and brittle crack-tip response in equimolar refractory high-entropy alloys, Acta Mater. 189 (2020) 174–187.
[8] P. Kumar, S.J. Kim, Q. Yu, J. Ell, M. Zhang, Y. Yang, J.Y. Kim, H.K. Park, A. M. Minor, E.S. Park, R.O. Ritchie, Compressive vs. tensile yield and fracture toughness behavior of a body-centered cubic refractory high-entropy superalloy Al0.5Nb1.25Ta1.25TiZr at temperatures from ambient to 1200 °C, Acta Mater. 245 (2023).
[9] O.N. Senkov, J.M. Scott, S.V. Senkova, D.B. Miracle, C.F. Woodward, Microstructure and room temperature properties of a high-entropy TaNbHfZrTi alloy, J. Alloys. Compd. 509 (20) (2011) 6043–6048.
[10] S. Wang, M. Wu, D. Shu, G. Zhu, D. Wang, B. Sun, Mechanical instability and tensile properties of TiZrHfNbTa high entropy alloy at cryogenic temperatures, Acta Mater. 201 (2020) 517–527.
[11] L.H. Mills, M.G. Emigh, C.H. Frey, N.R. Philips, S.P. Murray, J. Shin, D.S. Gianola, T.M. Pollock, Temperature-dependent tensile behavior of the HfNbTaTiZr multi-principal element alloy, Acta Mater. 245 (2023) 118618.
[12] O.N. Senkov, S. Gorsse, D.B. Miracle, High temperature strength of refractory complex concentrated alloys, Acta Mater. 175 (2019) 394–405.
[13] C. Liu, C. Gadelmeier, S. Lu, J. Yeh, H. Yen, S. Gorsse, U. Glatzel, A. Yeh, Tensile creep behavior of HfNbTaTiZr refractory high entropy alloy at elevated temperatures, Acta Mater. 237 (2022).
[14] C. Gadelmeier, Y. Yang, U. Glatzel, E.P. George, Creep strength of refractory high-entropy alloy TiZrHfNbTa and comparison with Ni-base superalloy CMSX-4, Cell Reports Phys. Sci. 3 (8) (2022).
[15] Z. Lin, E.J. Lavernia, F.A. Mohamed, High-temperature deformation in a Ta-W alloy, Acta Mater. 47 (4) (1999) 1181–1194.
[16] S. Yin, Y. Zuo, A. Abu-Odeh, H. Zheng, X.G. Li, J. Ding, S.P. Ong, M. Asta, R. O. Ritchie, Atomistic simulations of dislocation mobility in refractory high-entropy alloys and the effect of chemical short-range order, Nat. Commun. 12 (1) (2021) 4873.
[17] C. Lee, F. Maresca, R. Feng, Y. Chou, T. Ungar, M. Widom, K. An, J.D. Poplawsky, Y.C. Chou, P.K. Liaw, W.A. Curtin, Strength can be controlled by edge dislocations in refractory high-entropy alloys, Nat. Commun. 12 (1) (2021) 5474.
[18] F. Wang, G.H. Balbus, S. Xu, Y. Su, J. Shin, P.F. Rottmann, K.E. Knipling, J. C. Stinville, L.H. Mills, O.N. Senkov, I.J. Beyerlein, T.M. Pollock, D.S. Gianola, Multiplicity of dislocation pathways in a refractory multiprincipal element alloy, Science 370 (6512) (2020) 95–101.
[19] F. Maresca, W.A. Curtin, Mechanistic origin of high strength in refractory BCC high entropy alloys up to 1900K, Acta Mater. 182 (2020) 235–249.
[20] C.H. Belcher, B.E. MacDonald, D. Apelian, E.J. Lavernia, The role of interstitial constituents in refractory complex concentrated alloys, Prog. Mater. Sci. 137 (2023) 101140.
[21] N.J. Welch, M.J. Quintana, T.M. Butler, P.C. Collins, High-temperature oxidation behavior of TaTiCr, Ta4Ti3Cr, Ta2TiCr, and Ta4TiCr3 concentrated refractory alloys, J. Alloys. Compd. 941 (2023) 169000.
[22] D. Dickes, B. Öztürk, F. Baier, P. Berger, E.P. George, R. Völkl, M.C. Galetz, U. Glatzel, Surface hardening of TiZrNbHfTa high entropy alloy via oxidation, Corros. Sci. 217 (2023) 111159.
[23] T.M. Butler, O.N. Senkov, T.I. Daboiku, M.A. Velez, H.E. Schroader, L.G. Ware, M. S. Titus, Oxidation behaviors of CrNb, CrNbTi, and CrNbTaTi concentrated refractory alloys, Intermetallics 140 (2022) 107374.
[24] O.N. Senkov, J. Gild, T.M. Butler, Microstructure, mechanical properties and oxidation behavior of NbTaTi and NbTaZr refractory alloys, J. Alloys. Compd. 862 (2021) 158003.
[25] S. Sheikh, M.K. Bijaksana, A. Motallebzadeh, S. Shafeie, A. Lozinko, L. Gan, T. K. Tsao, U. Klement, D. Canadinc, H. Murakami, S. Guo, Accelerated oxidation in ductile refractory high-entropy alloys, Intermetallics 97 (2018) 58–66.
[26] F.C. Campbell, Elements of metallurgy and engineering alloys, ASM International, Materials Park, Ohio, 2008.
[27] C. Zhang, B.E. MacDonald, F.W. Guo, H.R. Wang, C.Y. Zhu, X. Liu, Y.W. Kang, X. C. Xie, Y.Z. Zhou, K.S. Vecchio, E.J. Lavernia, Cold-workable refractory complex concentrated alloys with tunable microstructure and good room-temperature tensile behavior, Scr. Mater. 188 (2020) 16–20.
[28] C. Zhang, H.R. Wang, X.Y. Wang, Q. Yu, C.Y. Zhu, M.J. Xu, S.T. Zhao, R. Kou, X. Wang, B.E. MacDonald, R.C. Reed, K.S. Vecchio, P.H. Cao, T.J. Rupert, E. J. Lavernia, Strong and ductile refractory high-entropy alloys with super formability, Acta Mater. 245 (2023).
[29] M.W. Decker, J.R. Groza, J.C. Gibeling, Creep properties of an extruded copper-8% chromium-4% niobium alloy, Mater. Sci. Eng. a-Struct.l Mater. Propert. Microstruct. Process. 369 (1–2) (2004) 101–111.
[30] G. Sahragard-Monfared, M. Zhang, T.M. Smith, A.M. Minor, E.P. George, J. C. Gibeling, The influence of processing methods on creep of wrought and additively manufactured CrCoNi multi-principal element alloys, Acta Mater. 261 (2023) 119403.
[31] G. Sahragard-Monfared, M. Zhang, T.M. Smith, A.M. Minor, J.C. Gibeling, Superior tensile creep behavior of a novel oxide dispersion strengthened CrCoNi multi-principal element alloy, Acta Mater. 255 (2023) 119032.
[32] Standard Guide for Combustion, Inert gas fusion and hot extraction instruments for use in analyzing metals, ores, and related materials, ASTM E3366-22, 2022.
[33] S.L. Wei, S.J. Kim, J.Y. Kang, Y. Zhang, Y.J. Zhang, T. Furuhara, E.S. Park, C. C. Tasan, Natural-mixing guided design of refractory high-entropy alloys with as-cast tensile ductility, Nat. Mater. 19 (11) (2020) 1175-+.
[34] Z. Lei, X. Liu, Y. Wu, H. Wang, S. Jiang, S. Wang, X. Hui, Y. Wu, B. Gault, P. Kontis, D. Raabe, L. Gu, Q. Zhang, H. Chen, H. Wang, J. Liu, K. An, Q. Zeng, T.G. Nieh,

Z. Lu, Enhanced strength and ductility in a high-entropy alloy via ordered oxygen complexes, Nature 563 (7732) (2018) 546–550.
[35] D. Cui, Y. Zhang, L. Liu, Y. Li, L. Wang, Z. Wang, J. Li, J. Wang, F. He, Oxygen-assisted spinodal structure achieves 1.5GPa yield strength in a ductile refractory high-entropy alloy, J. Mater. Sci. Techn. 157 (2023) 11–20.
[36] J.E. Dorn, Some fundamental experiments on high temperature creep, J. Mech. Phys. Solids. 3 (2) (1955) 85–116.
[37] O.D. Sherby, P.M. Burke, Mechanical behavior of crystalline solids at elevated temperature, Prog. Mater. Sci. 13 (1968) 323–390.
[38] H.J. Frost, M.F. Ashby, Deformation-mechanism maps: the plasticity and creep of metals and ceramics, Pergamon Press, Oxford, 1982.
[39] O.N. Senkov, A.L. Pilchak, S.L. Semiatin, Effect of cold deformation and annealing on the microstructure and tensile properties of a HfNbTaTiZr refractory high entropy alloy, Metallurg. Mater. Transact. A 49 (7) (2018) 2876–2892.
[40] U. Glatzel, F. Schleifer, C. Gadelmeier, F. Krieg, M. Müller, M. Mosbacher, R. Völkl, Quantification of Solid Solution Strengthening and Internal Stresses Through Creep Testing of Ni-Containing Single Crystals at 980°C, Metals, 2021.
[41] B. Pint, M. Ridley, S. Dryepondt, Ultimate FY23 vacuum creep testing facility operation report, Oak Ridge National Laboratory (ORNL), Oak Ridge, TN (United States), 2023.
[42] P. Pfizenmaier, A.S. Ulrich, M.C. Galetz, U. Glatzel, Tensile Creep Properties of Cr-Si Alloys at 980°C in Air—Influence of Ge and Mo Addition, Metals. (Basel) 11 (7) (2021) 1072.
[43] A. Jain, S.P. Ong, G. Hautier, W. Chen, W.D. Richards, S. Dacek, S. Cholia, D. Gunter, D. Skinner, G. Ceder, K.A. Persson, Commentary: the Materials Project: a materials genome approach to accelerating materials innovation, APL. Mater. 1 (1) (2013).
[44] B. Reppich, On the dispersion strengthening mechanisms in ODS materials, Internat. J. Mater. Res. 93 (7) (2002) 605–613.
[45] S.M. Chen, Z.J. Ma, S. Qiu, L.J. Zhang, S.Z. Zhang, R. Yang, Q.M. Hu, Phase decomposition and strengthening in HfNbTaTiZr high entropy alloy from first-principles calculations, Acta Mater. 225 (2022) 117582.
[46] G.Z. Voyiadjis, F.H. Abed, Microstructural based models for bcc and fcc metals with temperature and strain rate dependency, Mech. Mater. 37 (2) (2005) 355–378.
[47] X. Zhou, S. He, J. Marian, Cross-kinks control screw dislocation strength in equiatomic bcc refractory alloys, Acta Mater. 211 (2021) 116875.
[48] F. Maresca, W.A. Curtin, Theory of screw dislocation strengthening in random BCC alloys from dilute to "High-Entropy" alloys, Acta Mater. 182 (2020) 144–162.
[49] S.I. Rao, B. Akdim, E. Antillon, C. Woodward, T.A. Parthasarathy, O.N. Senkov, Modeling solution hardening in BCC refractory complex concentrated alloys: nbTiZr, Nb1.5TiZr0.5 and Nb0.5TiZr1.5, Acta Mater. 168 (2019) 222–236.
[50] S.I. Rao, C. Woodward, B. Akdim, O.N. Senkov, D. Miracle, Theory of solid solution strengthening of BCC chemically complex alloys, Acta Mater. 209 (2021) 116758.
[51] H. Suzuki, Solid solution hardening in body-centred cubic alloys, Dislocat.Solids 4 (1980) 191–217.
[52] R.E. Kubilay, A. Ghafarollahi, F. Maresca, W.A. Curtin, High energy barriers for edge dislocation motion in body-centered cubic high entropy alloys, npj, Computat. Mater. 7 (1) (2021) 112.
[53] K.K. Tseng, H.H. Huang, W.R. Wang, J.W. Yeh, C.W. Tsai, Edge-dislocation-induced ultrahigh elevated-temperature strength of HfMoNbTaW refractory high-entropy alloys, Sci. Technol. Adv. Mater. 23 (1) (2022) 642–654.
[54] C.B. Carter, D.B. Williams, Transmission Electron microscopy: Diffraction, imaging, and Spectrometry, Springer, 2016.
[55] S. Karthikeyan, G.B. Viswanathan, M.J. Mills, Evaluation of the jogged-screw model of creep in equiaxed γ-TiAl: identification of the key substructural parameters, Acta Mater. 52 (9) (2004) 2577–2589.
[56] G.B. Viswanathan, S. Karthikeyan, M.J. Mills, R.W. Hayes, Application of a modified jogged-screw model for creep of TiAl and α-Ti alloys, Metallurg. Mater. Transact. A 33 (2) (2002) 329–336.
[57] G.B. Viswanathan, R.W. Hayes, M.J. Mills, A study based on jogged-screw dislocations for high temperature creep in Ti alloys, Mater. Sci. Eng. 319-321 (2001) 706–710.
[58] B.M. Morrow, R.W. Kozar, K.R. Anderson, M.J. Mills, An examination of the use of the Modified Jogged-Screw model for predicting creep behavior in Zircaloy-4, Acta Mater. 61 (12) (2013) 4452–4460.
[59] C.R. Barrett, W.D. Nix, A model for steady state creep based on the motion of jogged screw dislocations, Acta Metallurgica 13 (12) (1965) 1247–1258.
[60] G.B. Viswanathan, V.K. Vasudevan, M.J. Mills, Modification of the jogged-screw model for creep of γ-TiAl, Acta Mater. 47 (5) (1999) 1399–1411.
[61] D.H. Cook, P. Kumar, M.I. Payne, C.H. Belcher, P. Borges, W. Wang, F. Walsh, Z. Li, A. Devaraj, M. Zhang, M. Asta, A.M. Minor, E.J. Lavernia, D. Apelian, R.O. Ritchie, Kink bands promote exceptional fracture resistance in a NbTaTiHf refractory medium-entropy alloy, Science 384 (6692) (2024) 178–184.